Linking initial microstructure and local response during quasistatic granular compaction

R. C. Hurley, J. Lind, D. C. Pagan, M. A. Homel, M. C. Akin, and E. B. Herbold

Phys. Rev. E **96**, 012905 — Published 24 July 2017

DOI: 10.1103/PhysRevE.96.012905

Linking initial microstructure and local response during quasi-static granular compaction

R. C. Hurley[1],* J. Lind[1], D. C. Pagan[1],† M. A. Homel[1], M. C. Akin[1], and E. B. Herbold[1]
[1] *Physical and Life Sciences, Lawrence Livermore National Laboratory, Livermore, CA 94550, USA*
(Dated: March 21, 2017)

We performed experiments combining three dimensional x-ray diffraction and x-ray computed tomography to explore the relationship between microstructure and local force and strain during quasi-static granular compaction. We found that initial void space around a grain and contact coordination number before compaction can be used to predict regions vulnerable to above-average local force and strain at later stages of compaction. We also found correlations between void space around a grain and coordination number, and between grain stress and maximum interparticle force, at all stages of compaction. Finally, we observed grains that fracture to have an above-average initial local void space and a below-average initial coordination number. Our findings provide: (1) a detailed description of microstructure evolution during quasi-static granular compaction; (2) an approach for identifying regions vulnerable to large values of strain and interparticle force; (3) methods for identifying regions of a material with large interparticle forces and coordination numbers from measurements of grain stress and local porosity.

PACS numbers: 45.70.Cc, 81.05.Rm, 91.60.-x

I. INTRODUCTION

Despite advances in understanding statistical relations between microstructure and material behavior, grain-scale links between local microstructure and mechanical response are not fully understood for granular media. Such links have been realized for other amorphous materials, such as metallic glasses, for which geometrically unfavorable structural motifs have been shown to correlate strongly with regions vulnerable to shear transformations [1]. Such links also play an important role in shear transformation zone theories for both amorphous and granular materials [2, 3]. The work detailed in this paper explores possible links between local microstructure and mechanical stress, strain, and force transmission in granular solids under quasi-static loading.

Extensive research has probed the relationship between microstructure statistics and material response during quasi-static loading of granular materials. For example, researchers have examined statistical relationships between fabric tensors and material response using theory [4], experiments [5], and simulations [6]. The development of stress-force-fabric relations [7] provided a direct analytical relationship between microstructure statistics and stress. These relations have been used in numerous quasi-static (e.g. [8]) and dynamic studies [9]. In addition to fabric tensors, vibrational modes, constructed from dynamical matrices which characterize sample-wide microstructure, have been used to locate regions of a material vulnerable to mesoscale structural rearrangements [10]. Network flow models have also been applied to initial packing microstructure to isolate grain clusters likely to participate in force chains [11]. All of these studies linked microstructure statistics or sample-wide metrics of microstructure to sample response.

In this work, we examine links between initial microstructure – porosity and coordination number – and local response of a granular packing undergoing quasi-static uniaxial compaction. We used far field high energy diffraction microscopy (ff-HEDM) and x-ray computed tomography (XRCT) to track grain strains, stresses, porosity, and contact fabric in a packing of 989 sapphire spheres subjected to uniaxial deformation within a cylinder. The experimental approach demonstrates a novel use of combined ff-HEDM and XRCT, well established in polycrystalline metals community [12, 13], for granular media. Mathematical and image-processing techniques were used to compute equivalent continuum strain, interparticle forces and grain-scale porosity, which is defined by the local void space surrounding each grain. Our results provide an approach for identifying, from a material's initial microstructure, regions vulnerable to large strains and interparticle forces.

This paper is structured as follows. In Sec. II, descriptions of the materials and experiment used to study granular compaction are given . The analysis of ff-HEDM and XRCT data for calculating grain strains, stresses, local porosity, coordination number, equivalent continuum strain, and interparticle forces is given in Sec. III. Section IV presents the correlations between grain stress and interparticle force, and between grain porosity and coordination number. In Sec. V, the links between a grain's initial porosity or coordination number, and the response of that grain due to sample compaction are investigated. We find that a grain's local porosity or coordination number prior to compaction serve as good predictors of the maximum force or local strain that the grain will experience at a later stage of compaction. The initial microstructure of grains that fracture during the compaction process is also discussed. Results and a discussion of topics for future investigations are given in Sec. VI.

* hurley10@llnl.gov
† Current address: Cornell High Energy Synchrotron Source, Ithaca, NY 14853, USA

II. MATERIAL AND EXPERIMENT

The granular sample studied in this work contained 989 single-crystal sapphire grains, 549 with diameter 193±2 μm and 440 with diameter 155± 4 μm. The two grain sizes were poured into a 10 mm tall Al-6061 cylinder with inner diameter 1.5 mm. Prior to pouring, a steel platen of diameter 1.5 mm was inserted into the bottom 5 mm of the cylinder. The platen, cylinder, and sample were placed in the compact load frame [14] present at 1-ID-E of the Advanced Photon Source (APS) at Argonne National Laboratory. The base of the compact load frame contained a load cell to measure force transmitted through the sample and platen. A loading piston was lowered into the top of the cylinder until contact was made with the granular sample, as determined by examining real-time transmission radiographs (described below). Figure 1a provides a schematic of the experimental setup.

Figure 1b shows a rendering of the granular sample constructed from segmented XRCT images (described below). Despite efforts to alternate pouring of grains with different diameters, significantly more grains of diameter 155 μm can be observed at the bottom of the sample while grains of diameter 193 μm are prominent at the top of the sample. Despite this layering of two nearly-monodisperse grain populations, crystallization is not evident in this image or in subsequent analysis. We note that the original purpose of using two grain sizes was to determine if local mechanical response differed for grains of a different size dispersed within the same sample. We proceeded with analysis of the current sample despite the segregated, rather than dispersed, mixing of grain size populations. We observed some differences in the probability distributions of measured quantities in each population of grain sizes, as discussed below. However, the microstructure-property relationships and associated correlations reported in Sec. IV and V hold for each population and when the populations are combined; therefore, they are described primarily for the combined data.

Before compacting the sample, the loading piston was lowered until the load cell registered a 10 N force and transmission radiographs simultaneously depicted no grain motion. The piston was then lowered at a constant velocity of 1 μm/s to desired load cell readings. Loading proceeded in ten steps to sample failure, with a single load reversal at an intermediate step to study reversibility. The sample stress increased with load until load step 6, after which grain fracture began to occur (discussed in Sec. V.3) and the sample stress dropped (discussed below). When desired load cell readings were reached, piston displacement was held constant while 1 mm tall slices of the sample were fully illuminated by a 51.996 keV monochromatic x-ray beam. During illumination, the sample was rotated twice through 360°, skipping 39° sections on opposite sides of the sample to avoid interference of the compact load frame's support posts with the x-ray source. During the first rotation, a Retiga 4000 CCD camera with 2048 x 2048 pixels and a 10x objective captured transmission radiographs as the rotation moved continuously through 0.25° increments. During the second rotation, a GE-41RT area detector with 2048 x 2048 pixels captured diffraction peaks as the rotation moved continuously through 0.25° increments.

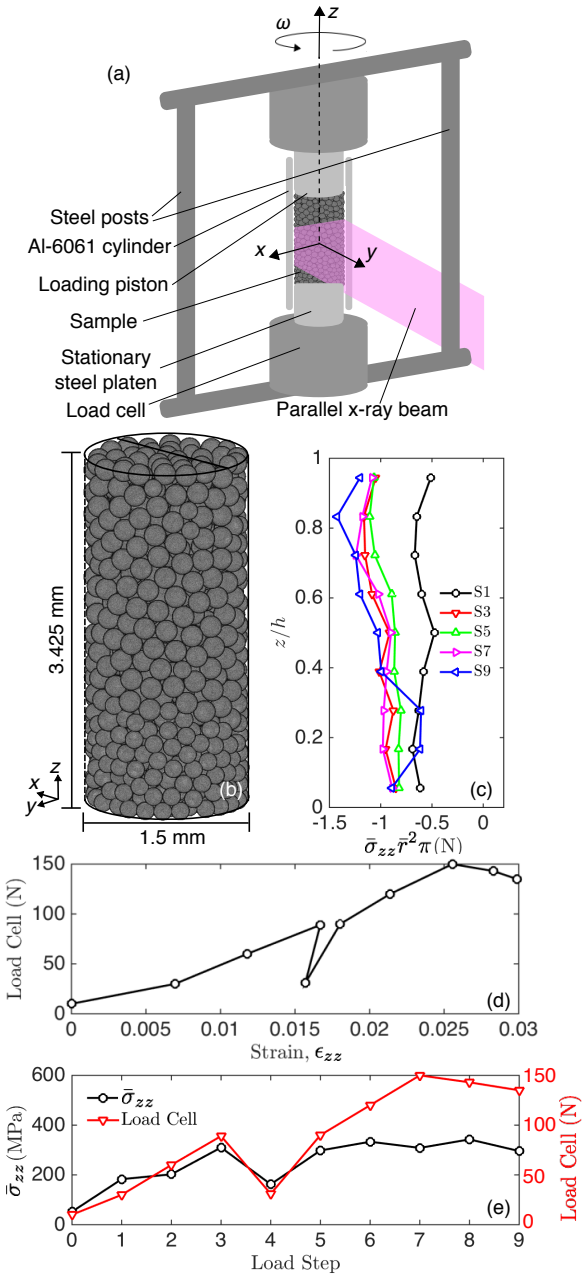

FIG. 1. (a) Schematic of the experimental setup, not to scale. (b) Rendering of granular sample at load step 0 from segmented XRCT image. (c) Average grain stress as a function of height in the sample at five load steps. (d) Load cell versus sample strain. (e) Comparison of load cell and volume-averaged sample stress computed from ff-HEDM data.

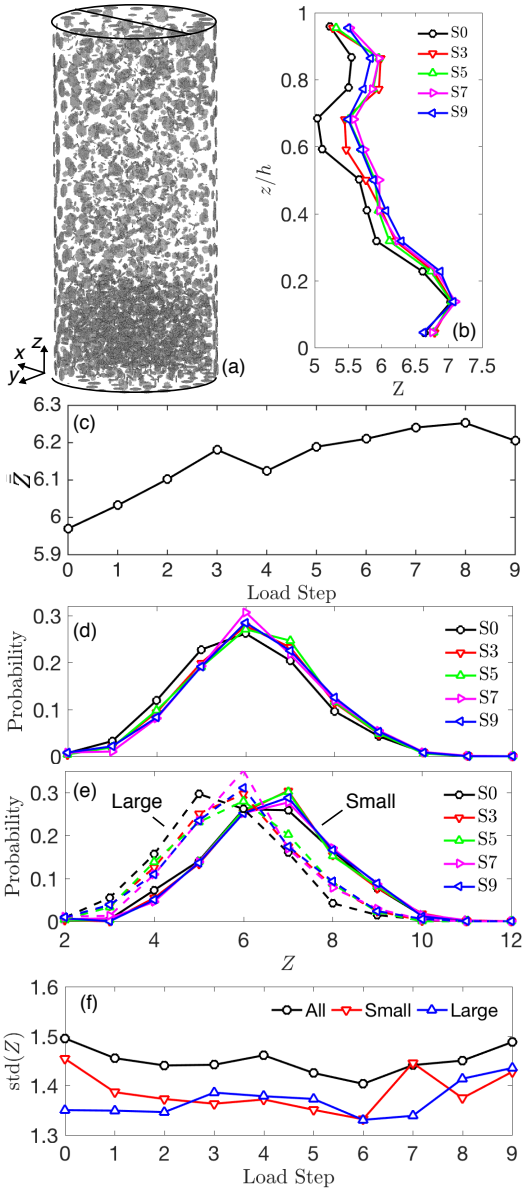

FIG. 2. (a) All image voxels belonging to a list of potential contact planes. (b) Coordination number as a function of height in the sample at five load steps. (c) Evolution of average coordination number of all grains in the sample. (d) Probability density of coordination number at five load steps. The letter S in the legend indicates load step. (e) Same as (d) but with small and large grain size populations separated. (f) Standard deviation of coordination number as a function of load step and grain size population. (d) and (e) share x-axes.

III. DATA ANALYSIS

III.1. XRCT and ff-HEDM

Raw XRCT reconstructions were generated at each load step from transmission radiographs by applying an inverse radon transform in Matlab to images from the Retiga 4000 CCD camera. Resulting XRCT images had a voxel size of 0.74 μm. Morphological operations including opening, watershed, and connected components search were performed in Matlab to segment individual grains. Grain volumes were determined by summing the voxels belonging to each grain, and centers of mass were determined by taking the unweighted average of voxel positions for each grain [15].

Separately, the grain position, average grain lattice strain, and grain lattice orientation were determined by optimizing the fit between diffraction peaks generated from a model (described in [12]) and those observed in images from the GE-41RT area detector. A ff-HEDM completeness score, used to determine which set of measurements to retain or eliminate, was determined for each grain by the ratio of the number of diffraction spots observed in the data with the predicted number attributed to individual crystal planes [12]. Setting a retention threshold of 0.6 for this completeness score appeared to eliminate grains with significant standard deviations in strain throughout the experiment and yielded a total of 828 to 950 grains, depending on load step, with usable grain strains. After average grain lattice strains were determined, average grain stresses were calculated by using single-crystal elastic moduli values of sapphire [16]: $C_{11} = 502$ GPa, $C_{12} = 161$ GPa, $C_{13} = 125$ GPa, $C_{14} = -19$ GPa, $C_{33} = 501$ GPa, and $C_{44} = 157$ GPa.

Figure 1d illustrates the load cell force versus sample strain during compaction. Sample strain is computed by $\epsilon_{zz} = -(h - h_0)/h_0$, where h is the current sample height and h_0 is the initial sample height, as determined from grain extents in the XRCT data. As evident from Fig. 1d, the sample was subjected to uniaxial compaction to failure, signaled by a drop in the load cell reading in Fig. 1d upon increasing strain after load step 7. A single load reversal was executed to investigate reversibility but will not be discussed further in this paper. Figure 1e compares the evolution of load cell force to the evolution of volume-averaged sample stress,

$$\bar{\sigma}_{zz} = \frac{1}{V_T} \sum_{i}^{N_p} \sigma_{zz}^{(i)} V_i, \tag{1}$$

where V_T is the total sample volume, including solid and pore space, between sample platens, N_p is the number of particles in the sample, $\sigma_{zz}^{(i)}$ is the average grain stress of grain i, derived from ff-HEDM, and V_i is the volume of grain i. Both curves in Fig. 1e follow similar trends, indicating sample softening in the last three load steps of the experiment. Softening in grain stress at load step seven precedes softening in load cell data, potentially indicating a small amount of load transfer around the grains due to piston-cylinder interaction. Figure 1c shows average grain stress as a function of height in the sample, multiplied by a term with length-squared units to prevent the confusing appearance of higher stresses in smaller grains. Each data point is computed by first dividing the sample into nine layers of equal height before volume-averaging grain stresses and radii (for calculation of the length-squared term) in each layer. Partial grain volumes in these layers were taken into account in the volume-

averaging. The curves illustrate that the sample is in a state of nearly uniform vertical compressive stress at low load (step 1, force ≈ 30 N) but progressively develops a stress gradient as load progresses due to grain-cylinder friction.

III.2. Coordination number and Porosity

The coordination number, Z, or number of contacts per grain, was determined by analyzing segmented XRCT images as follows. First, the sample boundaries were labeled with unique IDs in each image of segmented grains. Next, the 26-voxel neighborhood around each voxel in the image was evaluated for the presence of more than one grain ID. If two grain IDs (or a grain ID and a boundary ID) were present in a voxel's neighborhood, the voxel was added to a list of such voxels for that particular pair of IDs. After all voxels in an image were evaluated, contact planes were declared between a pair of IDs if their list contained a certain number of voxels, in this case equivalent to approximately 0.02% of a grain's volume. Coordination number was determined on a per-grain basis by summing the total number of such contacts per grain.

Figure 2a illustrates all voxels in an image of load step 0 that belonged to a list of potential contact planes. The bottom third of the sample is densely populated with contacts between the smaller grains, while the top two-thirds of the sample is less densely populated, mostly with contacts between the larger grains. Figure 2b illustrates the vertical distribution of coordination number, averaged in nine layers in the sample at five load steps. Higher coordination numbers are observed in the bottom third of the sample where the smaller grains are tightly packed. The top portion of the sample is primarily composed of larger grains. Sample-size effects, related to the ratio of grain to cylinder diameters, likely prevent this portion of the sample from achieving the same packing density as the bottom portion. Nevertheless, the coordination number is generally seen to increase with load at all heights. In the top half of the sample, the coordination number decreases slightly at the highest loads, which may occur because grains begin to fracture and significantly rearrange after load step 6.

Figure 2c illustrates the evolution of average coordination number in the sample, computed using both grain-grain and grain-boundary contacts, which follows trends in the load cell data for all steps except step 8. Figure 2d illustrates the probability density of coordination number at five load steps (following the convention of Fig. 2b in which the first load is step 0) through the experiment. A slight shift toward higher coordination numbers can be observed in the data at higher load levels. Figure 2e illustrates the same probability densities separately for the small and large grain size populations. As in Fig. 2b, the higher average coordination number for smaller grains is clear. However, both distributions can be observed to shift toward higher coordination numbers with load. Figure 2e illustrates that the standard deviation of coordination number is inversely related to volume-averaged sample stress, $\bar{\sigma}_{zz}$, from Fig. 1e at all load steps and is inversely related to macroscopic load at nearly all load steps. This holds for all grains and generally for the two grain size populations independently, although the large grain size population demonstrates some anomalous behavior between load steps 3 and 6. Therefore, in

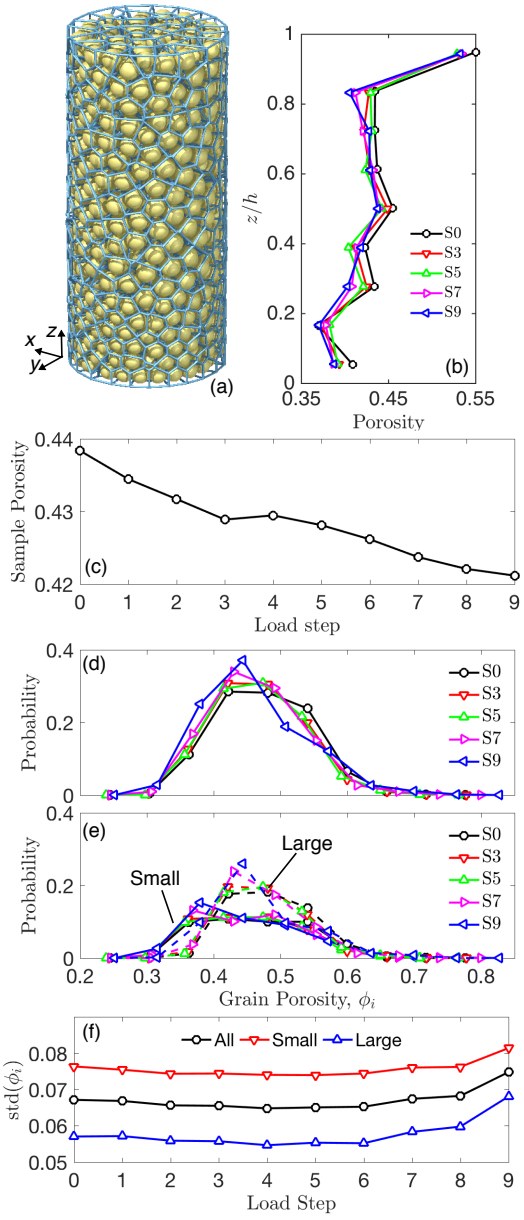

FIG. 3. (a) Rendering of the radical Voronoi tessellation for the sample at load step 0. Yellow spheres represent grains and the edges of the tessellation are rendered as blue lines. (b) Porosity as a function of height in the sample at five load steps. (c) Evolution of sample porosity with load step. (d) Probability density of porosity at five load steps. (e) Same as (d) but with small and large grain size populations separated. (f) Standard deviation of porosity as a function of load step and grain size population. (d) and (e) share x-axes.

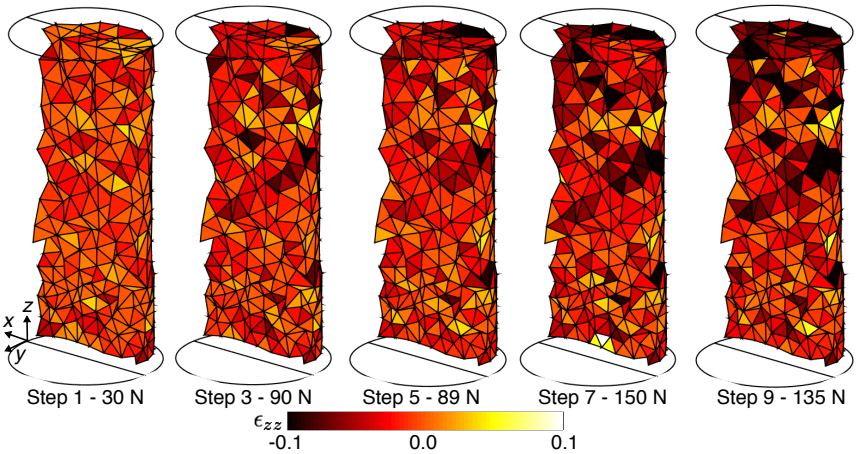

FIG. 4. ϵ_{zz} component of equivalent continuum strain, colored on a cutaway of the Delaunay triangulation for the sample at five load steps. Only tetrahedrons with nodes having physical location $y < 0$ are rendered in order to illustrate the interior of the sample.

addition to shifting toward higher coordination numbers at higher load levels, coordination number also becomes more homogeneous with macroscopic load until sample softening and grain fracture begin after step 6.

We used the software package `voro++` [17] to determine the radical Voronoi tessellation, also referred to as the Laguerre tessellation, for the sample at each load step. The radical Voronoi tessellation is a generalization of the standard Voronoi tessellation that prevents cell edges from intersecting grains in polydisperse packings by incorporating information about grain radii [18]. This tessellation has been employed in other studies of porosity and free volume in granular packings (e.g. [19]). From the radical Voronoi tessellation for the sample, we computed the local porosity around each grain, ϕ_i, by

$$\phi_i = 1 - \frac{V_i}{V_c}, \tag{2}$$

where V_c is the volume of the Voronoi cell enclosing grain i. Figure 3a illustrates a rendering of the radical Voronoi tessellation in POV-Ray [20] for the sample at load step 0, showing the grains as yellow spheres and the edges of the tessellation as blue lines. Figure 3b illustrates the vertical distribution of local porosity, averaged in nine layers in the sample at five load steps. Higher porosity is observed in the top layer due to the presence of the top piston, while slightly lower porosity is observed in the bottom third of the sample where the smaller grains are tightly packed. As the sample load increases, the porosity in each layer is observed to decrease, reaching its smallest value in most layers at load step 9. The lower average porosity for smaller grains may arise because the ratio of grain size to cylinder size permits a slightly more ordered packing at the bottom of the sample. Sample preparation may also have played a role in the observed porosity differences. Figure 3c shows that the porosity, evaluated for the entire sample, decreases with load step, increasing slightly only for the unload step 4.

Figure 3d illustrates the probability density of porosity at five load steps throughout the experiment. The shift in local porosity toward lower values can clearly be observed at higher load levels. Figure 3e illustrates the same probability densities but for the small and large grain size populations. Although the probability densities appear to have significantly different standard deviations, a shift in both distributions toward lower porosity values can be observed as at higher loads. Figure 3f demonstrates that the shift does not significantly affect the homogeneity of porosities until after load step 6: the standard deviation of grain porosities remains nearly constant until load step 7, suggesting that the distributions shift without dramatically changing shape.

III.3. Equivalent Continuum Strains and Forces

We used the radical Voronoi tessellation as a starting point for constructing equivalent continuum strains in the sample at each load step. First, we used the radical Voronoi tessellation at load step 0 to construct a generalized Delaunay triangulation by connecting groups of four mutual neighbors (a neighbor being defined as grains sharing a face in the Voronoi tessellation) into tetrahedrons. We then used these grain groups to construct tetrahedrons for the sample at all load steps. We computed the equivalent continuum strain in each tetrahedron by [21]

$$\epsilon_{ij} = \frac{1}{V_{tet}} \sum_{k=1}^{4} u_i^{(k)} a_j^{(k)}, \tag{3}$$

where V_{tet} is the tetrahedron volume, k is the tetrahedron's node index, $u_i^{(k)}$ is the displacement of node k from reference step 0. The vector $a_j^{(k)}$ is perpendicular to the tetrahedron face not containing node k, points toward the interior of the tetrahedron, and has a magnitude equal to the face area divided by the space dimension, in

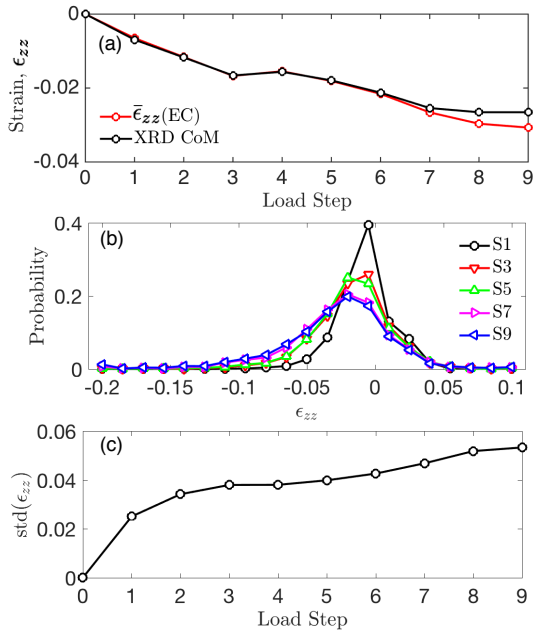

FIG. 5. (a) Comparison between volume-averaged equivalent continuum strain, $\bar{\epsilon}_{zz}$ (EC), and the sample strain (with legend entry XRD CoM) showing a close agreement of the two strain measures. (b) Probability density of ϵ_{zz} at five load steps. (c) Standard deviation of ϵ_{zz} as a function of load step.

this case 3. See [21] for the full derivation of this relationship.

Figure 4 illustrates the ϵ_{zz} component of the equivalent continuum strain in the sample, rendered on the sample's Delaunay triangulation, at five load steps throughout the experiment. Only tetrahedrons with physical location $y < 0$ are rendered for clarity and visualization of the internal volume of the sample. The strain at load step 1 is observed to be minimal and uniform, with some areas exhibiting slightly compressive or tensile strains. As loading progresses, dark areas, indicating large compressive strain, are observed with increasing prominence at the top of the sample. The primary analysis in this work, discussed in Sec. V, is partially driven by an interest in determining what aspects of the material's initial microstructure are responsible for these dark areas.

Figure 5a shows a comparison between the volume-averaged equivalent continuum strain, $\bar{\epsilon}_{zz}$ (EC), computed for the entire sample, and the sample strain as presented in Fig. 1c. The close agreement between the curves suggests that the strain computed by Eq. (3) is consistent with the continuum strain, as suggested independently by numerical studies [25]. Deviation of the curves at high loads occurs because our Voronoi tessellation does not account for grain fracture, which is concentrated in the last three load steps. Rather than using all grain fragments in the Voronoi tessellations after fracture, we used only the largest grain fragment passing the XRD retention threshold, or the last center of mass for grains with no constituents above the retention threshold. Figure 5b illustrates the probability density of ϵ_{zz} throughout the experiment. At load step 1, this probability density is narrow and peaks close to zero. At higher loads, the probability density is observed to flatten and extend to more negative values. Figure 5c illustrates the standard deviation of ϵ_{zz} as a function of load step. The standard deviation increases monotonically with load step except for load step 4, where it remains unchanged during unloading. This suggests that local strains become increasingly heterogeneous as loading progresses.

Interparticle forces were computed at each load step by solving the bi-objective optimization problem discussed in [22–24]. One objective function contained grain stresses determined from ff-HEDM, contact locations determined from XRCT, and the relationships between boundary forces on grains and grains' volume-averaged stresses. The other objective function contained contact locations and grain equilibrium equations. A solution was sought that falls near the "knee point" (e.g. see [26]) of the optimal tradeoff curve between the two objective functions, while obeying a sapphire-sapphire friction coefficient of 0.1 and a sapphire-aluminum friction coefficient of 0.4 [27]. This solution was obtained by using the software CVX [28] in Matlab®.

Figure 6 illustrates the normal forces, f_n, greater than twice the mean normal force, $\langle f_n \rangle$, for five load steps throughout the experiment. Forces are rendered as lines parallel to force vectors, centered at contact points, and scaled in length and thickness with force magnitude. The same scale for line thickness and length was used for all load steps. Grains corresponding to contact forces $f_n \geq 2\langle f_n \rangle$ are also rendered with 65% transparency and colored with stress ellipsoids [24] if their stresses were determined with sufficient completeness from the ff-HEDM analysis. The rendering corresponding to load step 1 in Fig. 6 illustrates that most grains have principal stresses close to zero and forces do not demonstrate discernible self-organization into force chains. The rendering corresponding to load step 3 illustrates the emergence of discernible force chains in the upper half of the sample, transmitting load vertically from the top piston into the sample, from the top piston into the side wall, and spanning horizontally across the sample. The remaining renderings illustrate significant changes in the force chains throughout loading, likely due to grain rearrangements and fracture. While fragmented grains become difficult to track, we can observe visual correlations between regions experiencing large compressive strains in Fig. 4 and those experiencing changes to force chains in the upper half of the sample. A few force chain structures are seen in all renderings from load step 3 onward or from load step 5 onward. A select few of these are highlighted with dashed red lines and suggest that portions of the force network are not affected by rearrangements caused by loading or grain fracture. Interestingly, the largest force magnitudes are observed in the bottom and top thirds of the sample. While the large force magnitudes in the top third are likely related to load transmission from the pis-

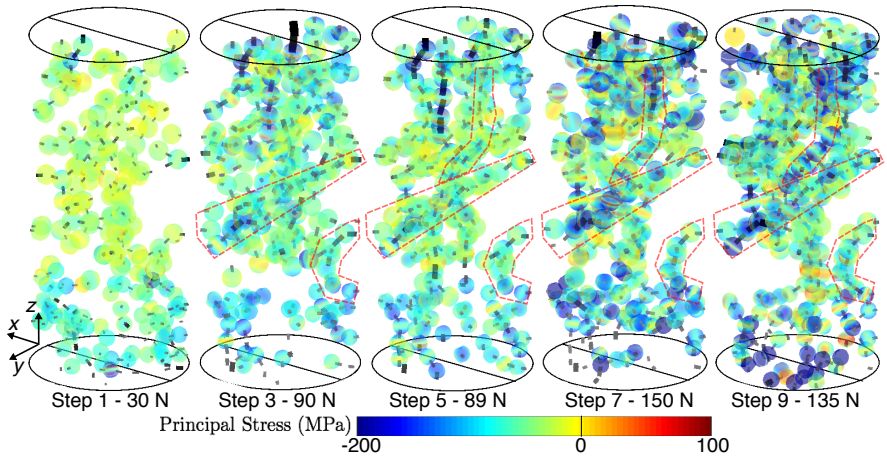

FIG. 6. Interparticle forces computed from measurements using techniques from [22–24] at five load steps. Black lines represent force vectors and are centered at contact points. These lines are scaled linearly in thickness and length according to force magnitude, using the same scale for all load steps. Only forces having normal magnitude $f_n \geq 2\langle f_n \rangle$ are rendered for clarity. Grains corresponding to these forces and having ff-HEDM completeness scores above the retention threshold are colored according to their principal stresses. Red dashed lines highlight force chains that are present in all future load steps. Many force chains visible in early load steps are not visible in later load steps.

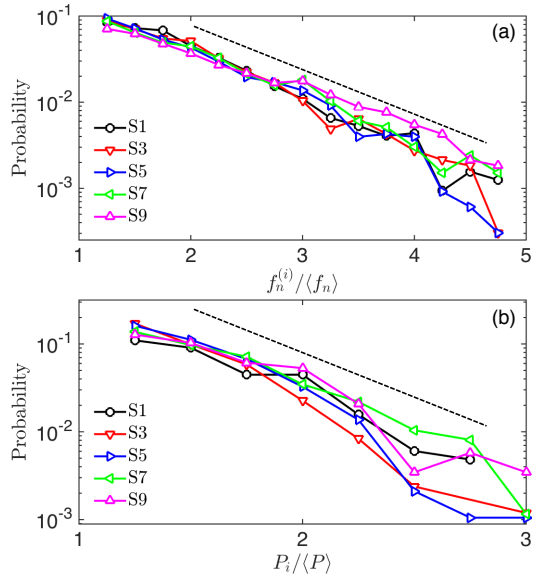

FIG. 7. (a) Probability density of normal force magnitudes demonstrate a roughly exponential decay above the mean at all load steps. (b) Probability density of mean grain pressures demonstrate a roughly exponential decay above the mean at all load steps.

ton into the sample and to the cylinder walls, the large force magnitudes in the lower third of the sample appear to occur in the grains with smaller diameters and may suggest some overconsolidation during packing. We do not further investigate this possibility here. We note that determining what aspects of initial microstructure determine the locations of the force chains seen in Fig. 6 is a major driver of the current research, a main subject of Sec. V, and a major research driver throughout the field of granular materials [10, 11].

Figure 7a illustrates the probability distribution of f_n above the mean for five load steps throughout the experiment. The probability distribution follows an exponential decay above the mean, consistent with numerous experimental and numerical studies [24, 29]. This distribution and that of mean grain pressure in Fig. 7b will be discussed in the next section.

IV. MEASUREMENT CORRELATIONS

There are several reasons why correlations between the variables introduced above are useful for interpreting experimental data. Mean grain pressure, $P_i = -\sigma_{jj}^{(i)}/3$, where i is the grain index and not an vector index, is a relatively simple calculation to make after grain strains are determined from ff-HEDM data. However, calculation of interparticle forces represents a significant numerical task, particularly for large grain assemblies, involving an optimization problem and a heuristic selection of a trade-off parameter [24, 26]. Nevertheless, interparticle forces are used to locate force chains (assumed to be contacts carrying $f_n \geq \langle f_n \rangle$) [24, 29, 30], to partition the force network into weak and strong networks for stress analysis [30], and to build models of failure and dynamics [31, 32]. Figure 8 illustrates P_i for grains with physical location $y < 0$ at five load steps throughout the experiment. Significant spatial variability can be observed, but, as for f_n in Fig. 6, maximal values of P_i are pronounced in the bottom and top thirds of the sample. Furthermore, Fig. 7b illustrates that P_i follows a roughly exponential decay above the mean at all load steps, similar to normal forces. These similarities between P_i and f_n suggests that there may be a useful correlation between mean grain stress and a grain's maximum interparticle force. We note that with our definition of P_i, positive values indicate com-

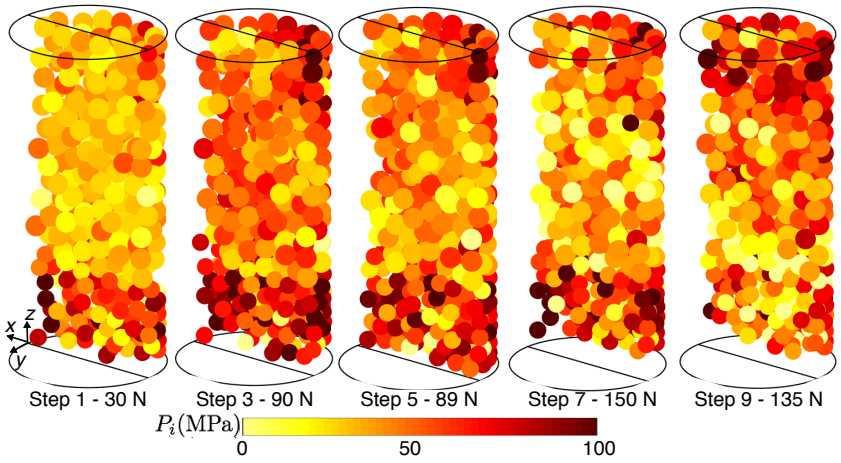

FIG. 8. Mean grain pressure computed for grains having a ff-HEDM completeness score above the retention threshold of 60%, shown for five load steps. Only grains having physical location $y < 0$ are rendered for clarity.

pression. This definition is for convenience of presenting P_i only, and does not extend to σ_{ij} or ϵ_{ij}, for which negative values indicates compression.

In Fig. 9, we demonstrate that P_i is indeed correlated with $\max(f_n)$ by plotting a density map of each grain's pressure and maximum force values at three load steps. Both grain-grain and grain-boundary forces were considered in calculating the maximum force on a grain. A dashed line is drawn through the data to highlight the trend in both data sets, although not to represent an actual fit to the data. A simple least-squares fit to the data was found to be excessively sensitive to outliers. Significant scatter in both P_i and the maximum f_n can be observed, particularly at higher loads, but the figures also illustrate that higher values of P_i typically correspond to grains with higher values of maximum f_n.

We further verify this finding by computing the correlation coefficient between P_i and $\max(f_n)$ for all N_p grains by

$$\mathrm{Corr}(\max(f_n), P_i) = \frac{\sum_i^{N_p}(\max(f_n)^{(i)} - \langle\max(f_n)\rangle)(P_i - \langle P_i\rangle)}{\sqrt{\sum_i^{N_p}(\max(f_n)^{(i)} - \langle\max(f_n)\rangle)^2}\sqrt{\sum_i^{N_p}(P_i - \langle P_i\rangle)^2}}, \tag{4}$$

where a superscript on $\max(f_n)^{(i)}$ was added to emphasize that the sum runs over all grains. A value of 0 indicates no correlation, a value of -1 indicates perfect negative linear correlation and a value of 1 indicates perfect positive linear correlation. Figure 11a illustrates this correlation coefficient at each load step. The correlation coefficient for all steps after step 0 ranges from 0.35 to 0.46, increasing slowly as sample compression proceeds. This curve confirms the positive correlation between P_i and $\max(f_n)$ that was suggested by Fig. 9, although the moderate value of the correlation coefficient highlights the presence of significant variability in the data. We note that the same trend in correlation coefficient also holds for the grain size populations independently, as shown in Fig. 11c.

This result is not trivial and many exceptions can be observed: several grains have smaller values of P_i despite larger values of maximum f_n, and vice versa. Nevertheless, the observed correlation may be useful for identifying regions of a material likely participating in force networks without the need for reconstructing the entire network. This could be particularly useful for samples for which XRCT is unavailable or for which a large number of grains makes force network reconstruction challenging. We note that all P_i values reflect measurement error inherent in ff-HEDM strain analysis (up to $\pm 1 \times 10^{-4}$ [12]) and thus some grains exhibiting negative P_i values may not actually be in a state of tension.

As with mean grain pressure, calculating the local porosity field is relatively simple once XRCT images have been binarized. A porosity map with similar spatial resolution to the map of ϕ_i may be constructed from a binarized XRCT image by averaging voxel values falling within certain averaging windows. However, calculating the coordination number requires segmenting XRCT images, a search through all image voxels, and volume-based voxel thresholding, as described in Sec. III.2. Figure 10 illustrates that grain porosity, ϕ_i, is inversely correlated with the coordination number, Z, at all load steps. A dashed line is again drawn through the data to highlight the trend in both data sets. There is significant scatter in ϕ_i for grains with a given Z since each

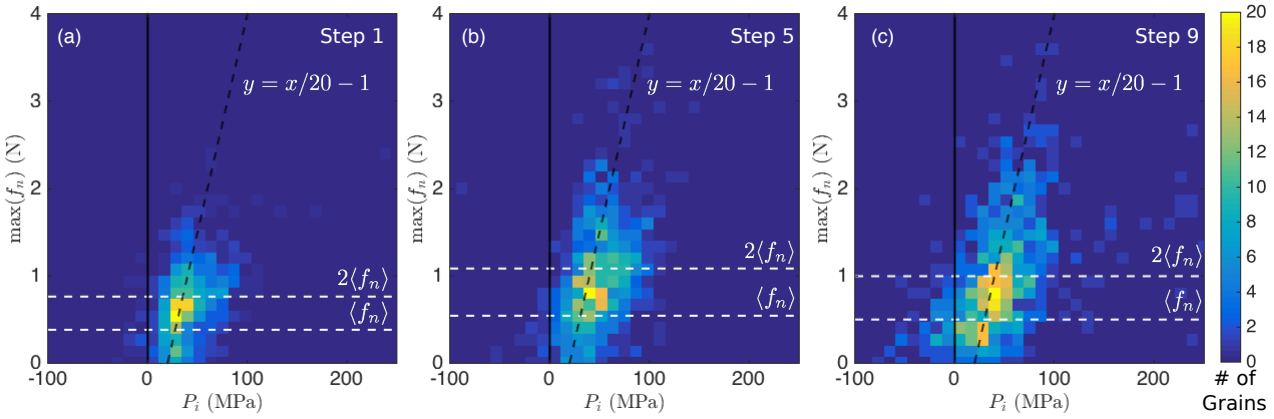

FIG. 9. Relationship between mean grain pressure, P_i, and the maximum force on a grain at load steps 1 (a), 5 (b), and 9 (c). Colors reflect the number of grains per square with the corresponding bivariate state. White horizontal dashed lines indicate the mean and two times the mean force at each load step. The black dashed line is a visual guide for correlation between variables, but not an actual fit to the data. Forces include those at both grain-grain and grain-boundary contacts.

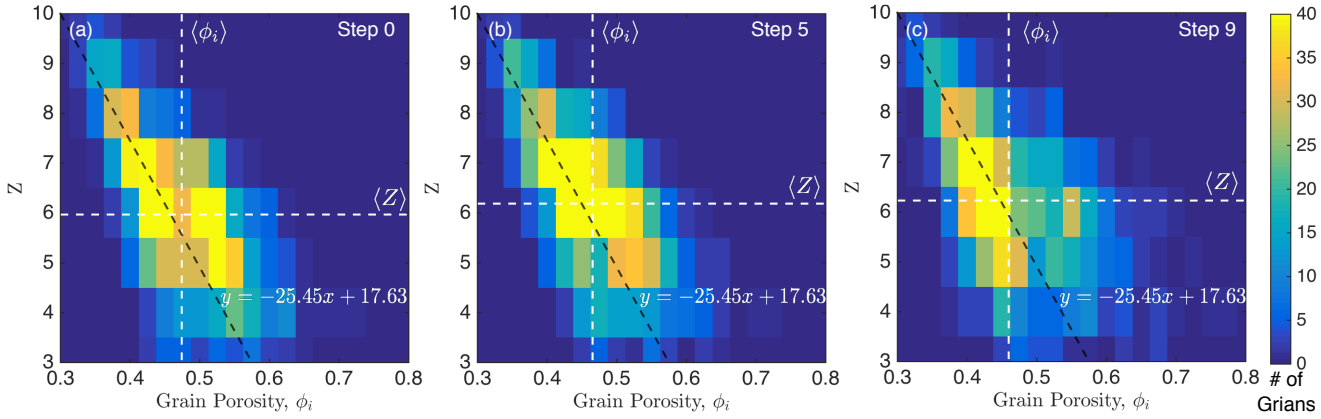

FIG. 10. Relationship between grain porosity, computed from the radical Voronoi tessellation, and grain coordination number, Z, at load steps 0 (a), 5 (b), and 9 (c). Colors reflect the number of grains per square with the corresponding bivariate state. The white vertical dashed line indicates the mean porosity in all cells of the radical Voronoi tessellation at each load step.

grain's local neighborhood is unique. Despite the scatter, a clear trend is observed in which grains with higher ϕ_i typically have lower Z, while grains with lower ϕ_i, typically have higher Z, since lower ϕ_i is typically associated with a tighter "caging" of a grain by its neighbors. This result is in agreement with other research [33] which has observed these trends close to the jamming transition. Below, ϕ_i and Z will also be shown to provide good statistical predictors of regions that experience extreme values of equivalent continuum strain and maximum interparticle force, suggesting that their evaluation at the beginning of compaction may help determine regions exhibiting important micromechanics at later stages of compaction.

In Fig. 11b, we illustrate the correlation coefficient between ϕ_i and Z at each load step. The correlation coefficient ranges from -0.68 to -0.55, confirming the relationship discussed above. The moderate value of the correlation coefficient again highlights the presence of significant variability in the data. We again note that these trends hold for the grain size populations independently, as shown in Fig. 11d. The weaker correlations for the large grain size populations may reflect sample-size limitations noted earlier.

V. LINKS BETWEEN MICROSTRUCTURE AND MECHANICAL RESPONSE

As noted in Sec. I, identifying links between microstructure and mechanical response is an important goal of research in granular and amorphous materials. One step toward achieving this goal would be the identification of features of a sample's initial microstructure, prior to loading, that correlate with regions of a material vulnerable to strain localization and high values of stress and interparticle force. In this section, we identify several features that provide such correlations. For brevity, we show only results for all grains but note that the observed correlations also hold for separate grain size populations.

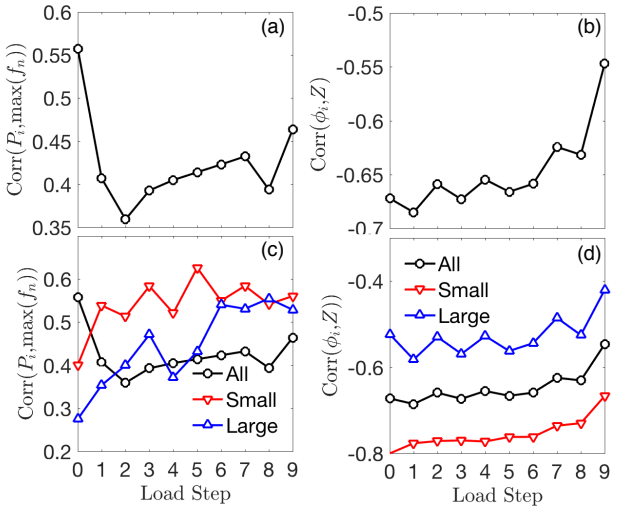

FIG. 11. (a) Correlation coefficient between P_i and max(f_n) at each load step. (b) Same as (a) but for ϕ_i and Z. (c) and (d) are the same as (a) and (b), respectively, but show curves for the separate grain size populations. (a) and (c), and (b) and (d), share x-axes.

V.1. Predicting Mechanics from Initial Porosity

Figure 12 illustrates the relationship between ϕ_i at load step 0 and max($f_n^{(i)}$), P_i, and $\epsilon_{zz}^{(i)}$ (EC) for each grain at load step 9. The grain-centered equivalent continuum strain, $\epsilon_{zz}^{(i)}$, is calculated as the average strain of tetrahedrons that have grain i as a vertex. Figure 12a suggests that grains with the lowest initial ϕ_i (at load step 0) tend to develop maximum f_n greater than the mean. Less clear from Fig. 12a, but still evident, is that grains with the highest initial porosity in the sample tend to develop maximum f_n that are less than grains with lower porosities. Figure 12b illustrates very little correlation between ϕ_i at load step 0 and P_i at the last stage of compaction. Figure 12c suggests that grains with the lowest initial ϕ_i tend to experience smaller compressive strain magnitudes, $\epsilon_{zz}^{(i)}$, in their local neighborhoods in later stages of compaction. Similarly, grains with the highest initial ϕ_i tend to experience higher compressive strain magnitudes in their local neighborhoods at later stages of compaction. This suggests that a primary deformation mechanism in this system is reduction of void space surrounding grains with an initially high ϕ_i.

In Fig. 13a, we show the probability that grains with a given ϕ_i at load step 0 exhibit forces greater than the mean force for five load steps throughout the experiment. For each load step, we computed probabilities by grouping grains into the bin to which their ϕ_i at load step 0 is closest. We then computed the number of grains in each bin whose maximum f_n is greater than $\langle f_n \rangle$ for that load step, and divided by the total number of grains in that bin. Each bin in Fig. 13 contained at least 45 grains, with those for the middle three bins containing over 250 grains. The horizontal dashed lines represent the same operation computed for all grains in the sample at each load step. Symbols on the ends of the dashed lines correspond to legend entries indicating the corresponding load step. The line without symbols corresponds to all load steps not captured by other lines.

The trend we alluded to in discussion of Fig. 12a is clearer upon inspection of Fig. 13a. Grains with initial ϕ_i less than the sample mean tend to experience forces $f_n > \langle f_n \rangle$ at a higher probability than do all sample grains. Similarly, grains with initial ϕ_i greater than the sample mean tend to experience forces $f_n < \langle f_n \rangle$ at a higher probability than do all sample grains. These trends hold at every load step of compaction. In Fig. 14a, we illustrate the extent to which this result holds as compaction progresses by plotting the correlation coefficient between a grain's ϕ_i at step 0 and max(f_n) at later steps, analogously to Eq. 4. The absolute value of the correlation coefficient decreases as compaction progresses, suggesting that a grain's initial porosity can be used to predict which grains are more or less likely to experience forces above or below the mean force at later stages of compaction; however, the predictive capability steadily decreases as compaction progresses. Nevertheless, this finding may provide a powerful tool for identifying, prior to loading, locations of a material that will feature force chains, an important pursuit in the study of granular materials (e.g., [34]). While this holds for uniaxial compaction, it may not hold for more complicated loading paths in which grain rearrangements play a prominent role in determining the mechanical response.

In Fig. 13b, we show the probability that grains with a given ϕ_i at load step 0 exhibit local equivalent continuum strains, $\epsilon_{zz}^{(i)}$, less (more compresive) than the mean sample strain, $\bar{\epsilon}_{zz}$. Again, the trend we alluded to in discussion of Fig. 12c is clearer upon inspection of this figure. Grains with initial ϕ_i less than the sample mean tend to experience $\epsilon_{zz}^{(i)} < \bar{\epsilon}_{zz}$ at a lower probability than all grains in the sample at any given load step. Similarly, grains with initial ϕ_i greater than the sample mean tend to experience $\epsilon_{zz}^{(i)} < \bar{\epsilon}_{zz}$ at a higher probability than all grains in the sample at any given load step. This implies that higher porosity regions are effectively more compliant than low porosity regions. The one exception to this finding occurs in load step 1, which appears to exhibit anomalous results for high porosity grains. These anomalous results occur for grains near the top piston that have high initial porosities and have not yet rearranged to fill large voids between the piston and grains.

Figure 14b illustrates the extent to which ϕ_i at step 0 predicts $\epsilon_{zz}^{(i)}$ as sample compaction progresses. Unlike the case of max(f_n) in Fig. 14a, for which the predictive power of ϕ_i at load step 0 diminished as compaction progressed, we observe ϕ_i at step 0 to become more strongly (negatively) correlated with $\epsilon_{zz}^{(i)}$ as compaction progresses, reaching maximum absolute values at load step 9. We therefore conclude that initial porosity prior to compaction can be used to predict how the local strain field begins to evolve upon loading, but can more accurately predict how the strain field continues to

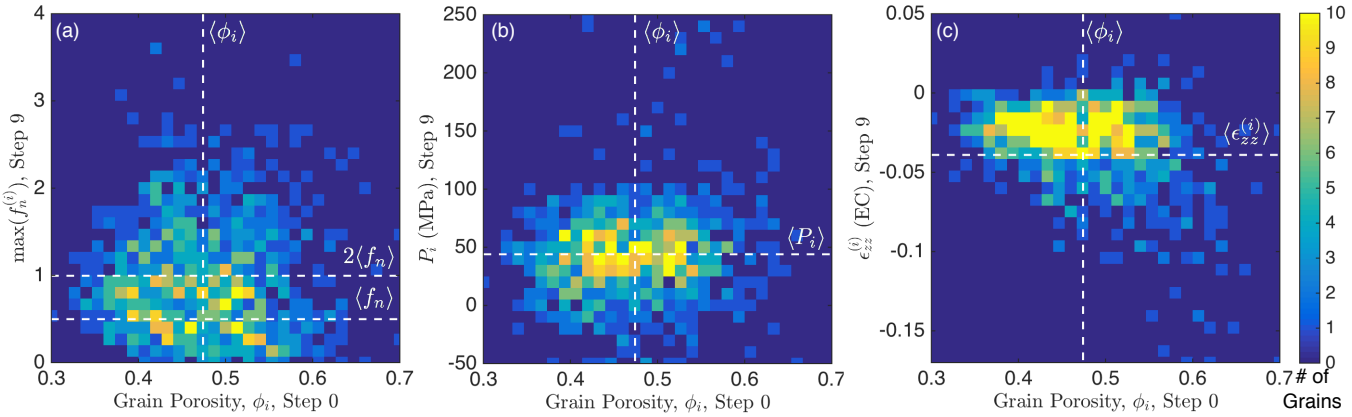

FIG. 12. Relationship between grain porosity, ϕ_i, at load step 0 and response variables (a) maximum interparticle force, (b) mean grain pressure, (c) grain-centered equivalent continuum strain, all at load step 9. Colors reflect the number of grains per square with the corresponding bivariate state. White dashed lines indicate mean values.

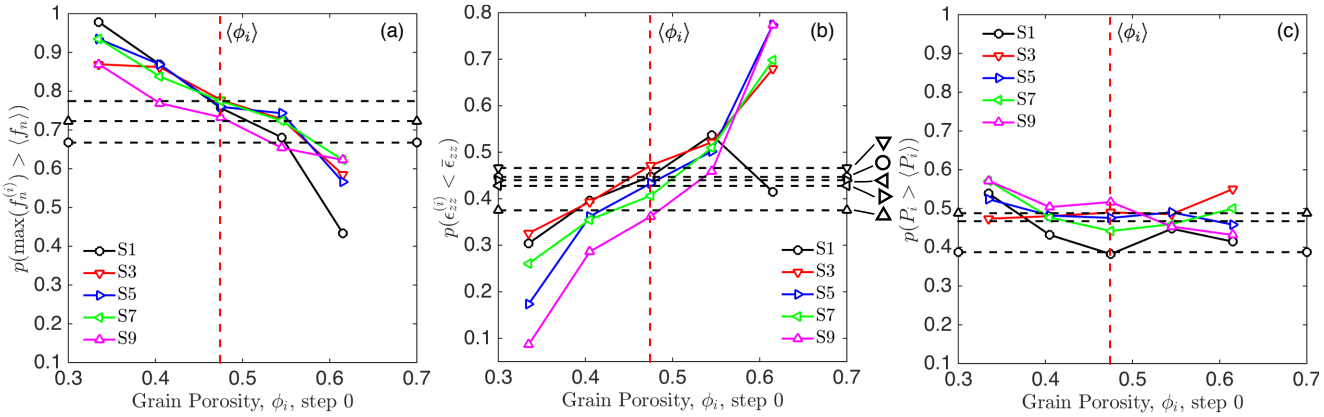

FIG. 13. (a) Probability that the maximum force on a grain will exceed the maximum force in the sample at five load steps, as a function of a grain's porosity at load step 0. (b) Probability that the ϵ_{zz} component of grain-centered strain will exceed (in magnitude) the sample strain at five load steps, as a function of a grain's porosity at load step 0. (c) Probability that the mean grain pressure, P_i, will exceed the mean grain pressure in the sample at five load steps, as a function of a grain's porosity at load step 0. The horizontal dashed lines represent means computed for all grains in the sample at each load step. Symbols on the ends of the dashed lines correspond to legend entries indicating the corresponding load step. Lines without symbols correspond to all load steps without symbols.

evolve as compaction progresses.

In Fig. 13, we show the probability that grains with a given ϕ_i at load step 0 experience a mean stress, P_i, exceeding the average throughout the sample. Unlike Figs. 13a and 13b, this figure does not convey trends that suggest initial porosity can be used to predict $p(P_i \geq \langle P_i\rangle)$. This finding is interesting in light of the results conveyed in Fig. 9, which shows a positive correlation between maximum interparticle force and P_i. Figure 14c confirms that the correlation coefficient of ϕ_i at step 0 and P_i at all load steps is low in magnitude and not of a consistent sign, varying between about -0.15 and 0.12 throughout compaction.

V.2. Predicting Mechanics from Initial Coordination Number

Figure 15 illustrates the relationship between coordination number at load step 0, Z_0, and $\max(f_n^{(i)})$, P_i, and $\epsilon_{zz}^{(i)}$ (EC) for each grain at load step 9. Figure 15a suggests that grains with the lowest Z_0 tend to be less likely to develop forces $f_n > \langle f_n\rangle$ by the end of compaction than grains with the highest Z_0. Figure 15b illustrates no discernible correlation between initial Z and final P_i. Finally, Fig. 15c suggests that grains with the highest initial Z tend to experience the least compressive strain in their local environment by the end of the compaction stage.

The trends alluded to in the preceding discussion are confirmed by Fig. 16. Figure 16a shows the probability that grains with a given Z at load step 0 exhibit forces

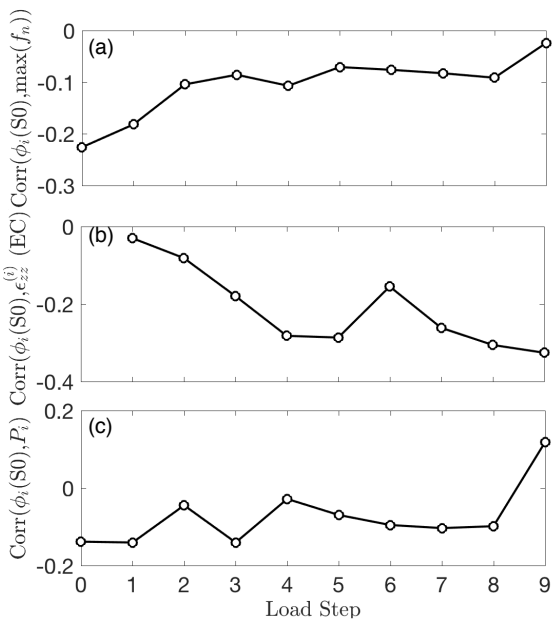

FIG. 14. Correlation coefficients between initial porosity and response at all load steps for (a) max(f_n), (b) $\epsilon_{zz}^{(i)}$ (EC), and (c) P_i.

greater than the mean force for five load steps throughout the experiment. For each load step, grains were binned and probabilities were calculated as they were for construction of Fig. 13, discussed above. There were greater than 30 grains in each bin except for $Z = 10$, which contained only eight grains. Bins $Z = 4$ through $Z = 7$ contained over 100 grains each. Grains with the lowest initial Z values are less likely than all sample grains to experience forces $f_n > \langle f_n \rangle$. Similarly, grains with the highest initial Z are more likely than all sample grains to experience forces $f_n > \langle f_n \rangle$. The value of Z at which these probabilities relative to the mean change sign is, as with ϕ_i, close to the mean value of Z at load step 0, or 5.97. This finding is partially explained by the correlation between Z and ϕ_i, but also by the fact that grains with lower (higher) Z have fewer (more) contacts and are therefore less (more) likely to experience large forces. It may also suggest that grains with fewer contact points are unstable to high forces and are therefore prone to rearrangements that decrease such loads. In Fig. 17a, we illustrate the extent to which this result holds as compaction progresses by plotting the correlation coefficient between a grain's Z at step 0 and max(f_n) at later steps. The correlation is most strongly negative at low loads, diminishing toward 0 at high loads, suggesting that the predictive power of initial coordination number in locating force chains diminishes as compaction proceeds. Nevertheless, this finding provides a link between a grain's initial coordination number, an important descriptor of its microstructure, and the mechanical response of that grain during uniaxial compaction.

Figure 16b shows the probability that grains with a given Z at load step 0 exhibit local equivalent continuum strains, $\epsilon_{zz}^{(i)}$, less than the mean sample strain, $\bar{\epsilon}_{zz}$. Grains with the lowest initial Z do not definitively demonstrate a higher probability of experiencing $\epsilon_{zz}^{(i)} < \bar{\epsilon}_{zz}$ than all grains in the sample. However, grains with the highest initial Z do demonstrate a lower probability of experiencing $\epsilon_{zz}^{(i)} < \bar{\epsilon}_{zz}$ than all grains in the sample. Grains with high initial Z therefore appear not to accommodate the void-filling displacement that would result in large values of compressive strain. Figure 17b illustrates the extent to which this result holds as compaction progresses. As in Fig. 14b, the correlation coefficient between initial coordination number and local strain increases as compaction progresses, suggesting that the accuracy of Z as a predictor of strain field evolution increases with load. This finding provides a link between a grain's initial coordination number and the mechanical response of that grain throughout uniaxial compaction. Both findings in Fig. 16a and 16b may provide a tool for identifying, prior to loading, locations of a material that will feature the force network or significant strain upon further compaction.

Figure 16c shows the probability that grains with a given Z at load step 0 experience a mean stress, P_i greater than the average throughout the sample. Similar to Fig. 13c, and unlike Figs. 16a and 16b, this figure does not convey trends that suggest initial coordination number can be used to predict $p(P_i \geq \langle P_i \rangle)$. Again, this finding is interesting in light of the results conveyed in Fig. 9. Taken together with Fig. 13c, this figure highlights that although maximum interparticle force and pressure, P_i, are positively correlated, care must be taken when making assumptions about one variable from the other. Figure 17c illustrates a positive correlation between Z_0 and P_i despite the lack of predictive power conveyed in Fig. 16c. We interpret this finding to suggest that the linear correlation coefficient is less sensitive to outlier behavior than the result conveyed in Fig. 16c. In Fig. 15b, the majority of the data for which Z_0 is between 5 and 7 indeed demonstrates a positive correlation between Z_0 and P_i; however, this correlation diminishes outside of this limited range. Thus, care must also be taken when interpreting results from either Figs. 16 or 17 in isolation.

V.3. Predicting Fracture from Initial Porosity and Coordination Number

We now briefly discuss the initial state of grains of that undergo fracture during the compaction process. Through analysis of reconstructed XRCT images, we identified a total of 27 grains that experience some fragmentation during sample compaction. Of those 27 grains, 23 appear to experience minor fractures close to contact points, or fractures that do not appear to result in a change in contact state or a separation of fragmented pieces. Many of these grains continue to have ff-HEDM completeness values above the threshold needed to retain them for analysis. Four of the 27 grains experience substantial fractures that appear to render them unable to bear any significant load. No portion of these four grains

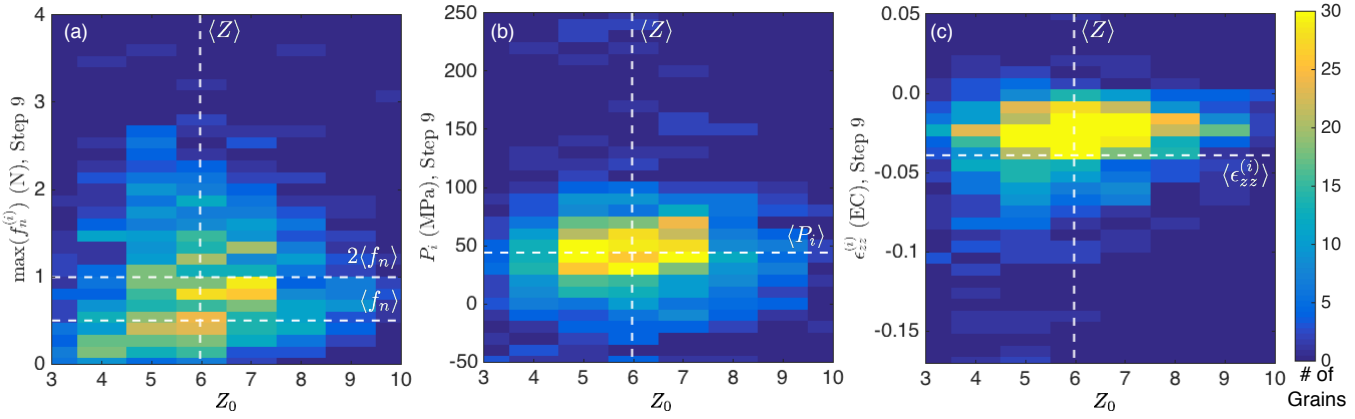

FIG. 15. Relationship between grain coordination number, Z, at load step 0 and response variables (a) maximum interparticle force, (b) mean grain pressure, (c) grain-centered equivalent continuum strain, all at load step 9. Colors reflect the number of grains per square with the corresponding bivariate state. White dashed lines indicate mean values throughout the sample.

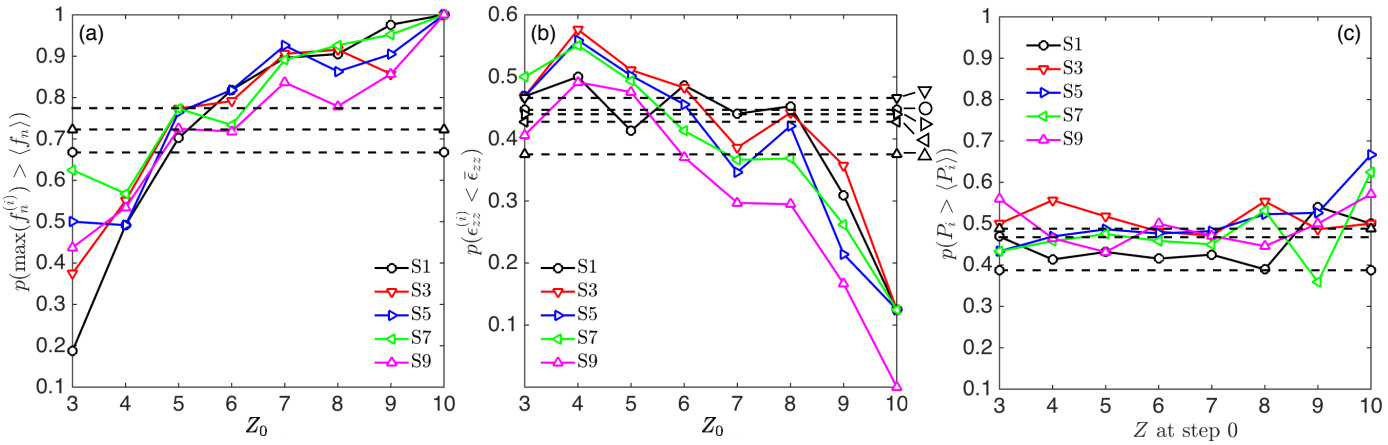

FIG. 16. (a) Probability that the maximum force on a grain will exceed the maximum force in the sample at five load steps, as a function of a grain's coordination number at load step 0. (b) Probability that the ϵ_{zz} component of grain-centered strain will be below (more compressive than) the mean sample strain at five load steps, as a function of a grain's coordination number at load step 0. (c) Probability that the mean grain pressure, P_i, will exceed the mean grain pressure in the sample at five load steps, as a function of a grain's coordination number at load step 0. The horizontal dashed lines represent means computed for all grains in the sample at each load step. Symbols on the ends of the dashed lines correspond to legend entries indicating the corresponding load step. Lines without symbols correspond to all load steps without symbols.

have sufficient volume to generate ff-HEDM completeness scores exceeding the retention threshold.

Figure 18a illustrates the initial microstructure of all grains in $\phi_i - Z$ space. The initial state of grains that experience fracture during sample compaction are highlighted with larger symbols of two types: one signifying those that appear to be load-bearing (LB) after fracture and one signifying those that appear to be non-load-bearing (NLB) after fracture. Figure 18b illustrates the probability (in percent, computed by count divided by initial grain count) that a grain in the sample will fracture during the compaction process as a function of grain porosity at load step 0. Of the 27 grains experiencing some level of fracture, 24 have initial grain porosity equal to or greater than the average porosity of all grains at load step 0. Figure 18c illustrates the probability (in percent) that a grain in the sample will fracture during the compaction process as a function of coordination number at load step 0. Of the 27 grains experiencing some level of fracture, 21 have initial coordination number equal to or less than the mean. These findings suggest that there may be links between a grain's initial microstructure and the probability it will experience fracture during uniaxial compaction. Such information could be valuable for identifying regions of a material likely to experience significant force chain or grain rearrangements due to fracture during compaction. For brevity, we reserve further investigation of fracture processes in this sample for future work.

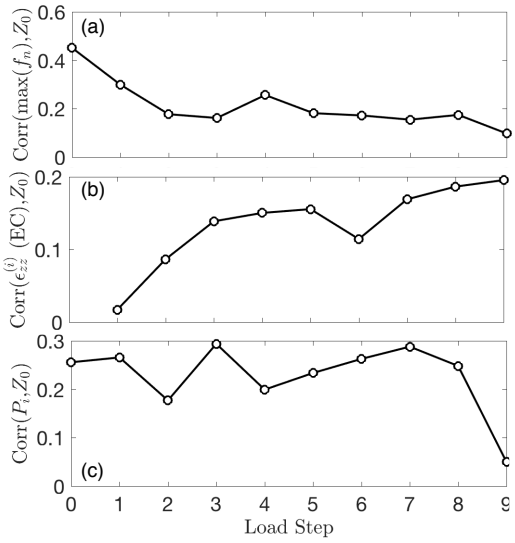

FIG. 17. Correlation coefficients between initial coordination number and response at all load steps for (a) $\max(f_n)$, (b) $\epsilon_{zz}^{(i)}$ (EC), and (c) P_i.

VI. DISCUSSION AND CONCLUSIONS

We have used ff-HEDM and XRCT to explore microstructure in a sample of sapphire spheres subjected to uniaxial compaction. We have related initial microstructure of a grain, prior to compaction, to mechanical response in its neighborhood at a later stage of compaction. We showed that an approach exists for identifying, from a granular material's initial microstructure, regions that are vulnerable to large strains and interparticle force. These results are an important step toward linking microstructure and mechanical response in granular solids, a major driver of research in the field (e.g., [10, 11]). These links between microstructure and local response may find important applications in predicting a material's performance prior to loading and in designing materials with microstructures tailored to exhibit desired mechanical responses. However, the results in this paper also highlight the difficulty in establishing useful microstructure-response relationships by illustrating that some such relationships have diminishing predictive power as material deformation progresses. Extending microstructure-property relationships to more varied loading conditions and materials should involve a combination of further experiments and simulations, and an investigation of other measures of structure and response, such as the fabric tensor and other stress measures. Crystalline sphere packings with no variation in porosity or coordination number, and polycrystalline grain packings with no porosity, should also be investigated since they would likely exhibit a breakdown of the microstructure-response links reported in this paper. We leave a full investigation of these cases to future work.

In the course of our analysis, we also showed that measurements of grain stress and local porosity from ff-HEDM and XRCT images are correlated with calculated interparticle forces and grain coordination number at all stages of compaction. These results may prove to be insightful for other loading conditions and grain shapes, and have been introduced to illustrate how meaningful, but computationally intensive, response and microstructure metrics can be obtained from simpler measurements. Finally, we provided a preliminary analysis of grain fracture that suggests that a grain's initial microstructure may constrain its likelihood of fracturing during compaction.

To summarize, the main findings of this work are:

1. Positive correlation exists between grain pressure and maximum inter-particle force throughout uniaxial compaction

2. Negative correlation exists between local porosity and coordination number throughout uniaxial compaction;

3. Local porosity and a grain's initial coordination number can be used to predict the location of force chain development at low loads, with predictive power diminishing as compaction progresses;

4. Local porosity and a grain's initial coordination number can be used to predict the location of large strains throughout compaction, with predictive power increasing as compaction progresses;

5. Combining ff-HEDM and XRCT provides a unique capability of probing various aspects of microstructure evolution and microstructure-response relationships in granular solids.

ACKNOWLEDGEMENTS

The authors thank R. Crum for valuable discussions. The authors acknowledge the Advanced Photon Source (APS) for synchrotron beamtime under proposal GUP-45260. Use of APS, an Office of Science User Facility opoerated for the U.S. Department of Energy (DOE) Office of Science by Argonne National Laboratory, was supported by the U.S. DOE under Contract No. DE-AC02-06CH11357. R.C.H. and E.B.H. acknowledge support from Lawrence Livermore National Laboratory's (LLNL) Laboratory Directed Research and Development (LDRD) program under grant number 17-LW-009. All authors acknowledge support from LLNL's LDRD program under grant number 16-ERD-010. This work was performed under the auspices of the U. S. DOE by LLNL under Contract DE-AC52-07NA27344.

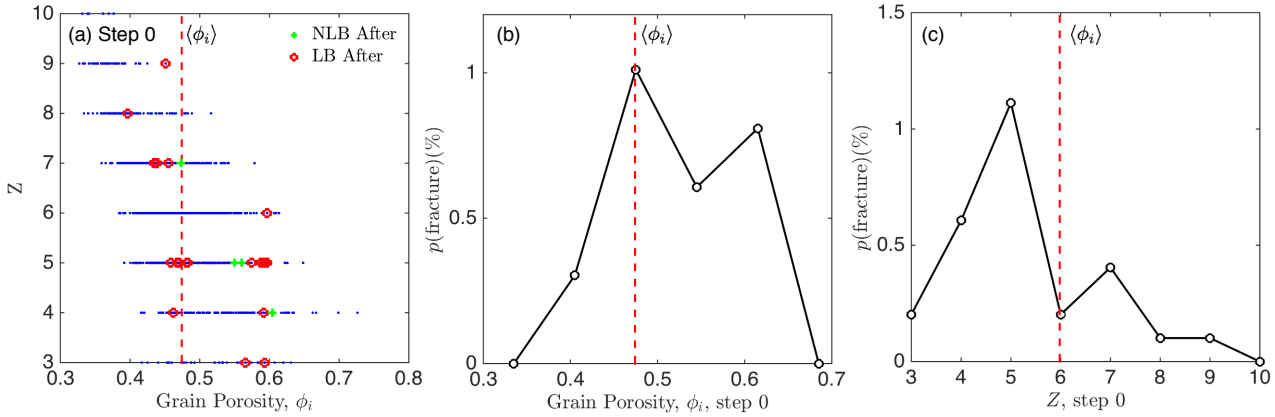

FIG. 18. (a) Grain porosity versus coordination number for all grains at load step 0. Symbols indicated in the legend represent grains that experience fracture rendering them non-load-bearing (NLB) or load-bearing (LB), as determined from visual analysis of unsegmented XRCT images. (b) Probability that a grain fractures at some stage of compaction as a function of grain porosity at load step 0. (c) Probability that a grain fractures at some stage of compaction as a function of coordination number at load step 0. Dashed lines in all figures indicate mean values throughout the sample.

[1] J. Ding, S. Patinet, M. L. Falk, Y. Cheng, and E. Ma, Proceedings of the National Academy of Sciences **111**, 14052 (2014).
[2] M. Falk and J. Langer, Physical Review E **57**, 7192 (1998).
[3] C. K. Lieou and J. Langer, Physical Review E **85**, 061308 (2012).
[4] M. M. Mehrabadi, S. Nemat-Nasser, and M. Oda, International Journal for Numerical and Analytical Methods in Geomechanics **6**, 95 (1982).
[5] M. Oda, S. Nemat-Nasser, and J. Konishi, Soils and foundations **25**, 85 (1985).
[6] C. Thornton and D. Barnes, Acta Mechanica **64**, 45 (1986).
[7] L. Rothenburg and R. Bathurst, Geotechnique **39**, 601 (1989).
[8] H. Ouadfel and L. Rothenburg, Mechanics of Materials **33**, 201 (2001).
[9] E. Azéma and F. Radjai, Physical review letters **112**, 078001 (2014).
[10] M. L. Manning and A. J. Liu, Physical Review Letters **107**, 108302 (2011).
[11] A. Tordesillas, S. T. Tobin, M. Cil, K. Alshibli, and R. P. Behringer, Physical Review E **91**, 062204 (2015).
[12] J. Bernier, N. Barton, U. Lienert, and M. Miller, The Journal of Strain Analysis for Engineering Design **46**, 527 (2011).
[13] J. Oddershede, S. Schmidt, H. F. Poulsen, H. O. Sørensen, J. Wright, and W. Reimers, Journal of Applied Crystallography **43**, 539 (2010).
[14] https://www1.aps.anl.gov/Sector-1/1-ID/Infrastructure/Compact-load-frame.
[15] J. Lind, M. C. Akin, and D. C. Pagan, Acta Geotechnica (2017), in review.
[16] W. Duan, B. B. Karki, and R. M. Wentzcovitch, American Mineralogist **84**, 1961 (1999).
[17] C. Rycroft, Lawrence Berkeley National Laboratory (2009).
[18] A. Gervois, L. Oger, P. Richard, and J. P. Troadec, in *International Conference on Computational Science* (Springer, 2002) pp. 95–104.
[19] J. M. Rieser, C. P. Goodrich, A. J. Liu, and D. J. Durian, Physical review letters **116**, 088001 (2016).
[20] "Persistence of vision pty. ltd." [Compute Software]. http://www.povray.org/download (2004).
[21] K. Bagi, Mechanics of materials **22**, 165 (1996).
[22] R. Hurley, E. Marteau, G. Ravichandran, and J. E. Andrade, Journal of the Mechanics and Physics of Solids **63**, 154 (2014).
[23] R. Hurley, K. Lim, G. Ravichandran, and J. Andrade, Experimental Mechanics **56**, 217 (2016).
[24] R. Hurley, S. Hall, J. Andrade, and J. Wright, Physical Review Letters **117**, 098005 (2016).
[25] K. Bagi, International Journal of Solids and Structures **43**, 3166 (2006).
[26] S. Boyd and L. Vandenberghe, *Convex optimization* (Cambridge university press, 2004).
[27] E. R. Dobrovinskaya, L. A. Lytvynov, and V. Pishchik, *Sapphire: material, manufacturing, applications* (Springer Science & Business Media, 2009).
[28] M. Grant, S. Boyd, and Y. Ye, "Cvx: Matlab software for disciplined convex programming," (2008).
[29] F. Radjai, M. Jean, J.-J. Moreau, and S. Roux, Physical review letters **77**, 274 (1996).
[30] F. Radjai, D. E. Wolf, M. Jean, and J.-J. Moreau, Physical review letters **80**, 61 (1998).
[31] A. Tordesillas and M. Muthuswamy, Journal of the Mechanics and Physics of Solids **57**, 706 (2009).
[32] A. H. Clark, A. J. Petersen, and R. P. Behringer, Physical Review E **89**, 012201 (2014).
[33] L. E. Silbert, Soft Matter **6**, 2918 (2010).
[34] Q. Lin and A. Tordesillas, Journal of Industrial and management optimization **10**, 337 (2014).